Supplementary Information

Skin-like quasi-solid-state electrolytes for spontaneous zinc-ion dehydration toward ultra-stable zinc-iodine batteries

*Shaochong Cao, Aiwen Zhang, Huayi Fang, Bingjian Feng, Yongshuai Liu, Pengshu Yi, Shan He, Zhouhong Ren, Longli Ma, Wenyi Lu, Mingxin Ye, and Jianfeng Shen**

* Corresponding Authors: jfshen@fudan.edu.cn

Contents

Supplementary Methods

1.1Materials.

4,4',4''-(1,3,5-triazine-2,4,6-triyl)trianiline (TAPT, 97%) and 1,3,5-triformylbenzene (TFB, 97%) were obtained from Shanghai Tensus Biotech Co., Ltd. Iodine, poly(vinylidene 470 fluoride) (PVDF, average Mw ~400000), nmethyl-2-pyrrolidone (NMP, 99%), $ZnSO_4 \cdot 7H_2O$, potassium hydroxide (KOH), acetic acid (CH_3COOH, 99.8%), and DMSO (99.7%) was provided by Shanghai Aladdin Biochemical Technology Co., Ltd. Poly (*p*-phenylene terephthalamide) (PPTA) was obtained from Dupont-Toray, Co., Ltd. Active carbon (AC, XFP06, 2000 mg/g of the iodine value) were obtained from the Nanjing/Jiangsu XFNANO Materials Tech Co., Ltd. Zinc foil (~0.1 mm), copper foil (~0.015 mm), and titanium foil (~0.03 mm) were purchased from Shenzhen Kejing Technology Co., Ltd. Glass fiber (GF/D) was purchased from Whatman. All chemicals were used directly without any post-processing unless otherwise stated.

1.2 Fabrication.

1.2.1 Preparation of I_2@Active carbon (I_2@AC) powders. I_2@AC were prepared by a facile room-temperature "solution-adsorption" method.[1] Briefly, 1 g iodine was first added in 200 mL of water and stirred for 4 h at room temperature. Then, 1 g active carbon was added and stirred thoroughly for 12 h. The mixture was centrifuged and dried.

1.2.2 Fabrication of iodine cathode. I_2@AC, PVDF binder and Super P were mixed in N methyl pyrrolidone (NMP) at a ratio of 8:1:1 and stirred for 3 h. The slurry was then uniformly coated onto the titanium foil (1.2×1.2 cm^2). Finally, the iodine cathodes were dried under vacuum at 40°C for 12 h. The mass loading of iodine was calculated as ~1.0 mg cm^{-2}.

1.2.3 Fabrication of PPTA hydrogel. Typically, 1 g of PPTA nanofiber were dissolved in 50 mL of DMSO with 0.5 g of KOH. A homogeneous aramid fiber DMSO solution was obtained after stirring at room temperature for 5 days. The as-prepared solution was cast onto a glass plate with a 200 μm thickness coating machine and subsequently immersed in deionized water for phase inversion process. The dark red

PPTA solution gradually becomes transparent and detaches from the glass plate to form a free-standing hydrogel. PPTA quasi-solid electrolyte (QSSE) was obtained by penetration diffusion of hydrogel under a concentration gradient in 2 M aqueous $ZnSO_4$ solution (Electrolyte content 98.8%).

1.2.4 Fabrication of skin-like quasi-solid-state electrolyte (skin-QSSE). COF nanolayers were prepared by in situ interfacial synthesis on the PPTA hydrogels surface to further obtain the skin-QSSE. 10 mL of a mixture consisting of amine monomer (0.2 w/v%, 4,4',4''-(1,3,5-triazine-2,4,6-triyl)trianiline, TAPT), acetic acid (0.2 mM), and deionized water was poured onto the surface of the PPTA hydrogel. The amine monomer solution on the hydrogel surface was removed after 5 min. then 10 mL 1,3,5-triformylbenzene (TFB, 0.2 w/v%) *n*-hexane solution was poured on the hydrogel surface to react for 10 min. Finally, the prepared COF-PPTA hydrogels were immersed in aqueous acetic acid (2.5 mmol) for 72 h at room temperature. The skin-QSSE was obtained by penetration diffusion of COF-PPTA hydrogel under a concentration gradient in 2 M aqueous $ZnSO_4$ solution.

1.3 Material characterizations.

Thermogravimetric analysis (TGA) was used to determine the iodine loading with a TG-DSC analyzer (NETZSCH, STA 449 F3, Germany) with a heating rate of 10 °C/min. X-ray diffraction (XRD) measurements were measured by MiniFlex600 diffractometer with Cu $K\alpha$ radiation (λ = 0.154 nm), and the diffraction data was collected at a step mode (2° min^{-1}) over the angular range of 3–50°. Bruker VERTEX 70v (Germany) was employed to acquire Fourier transform infrared (FT-IR) spectroscopy. Thermo Fisher machine (ESCALAB 250Xi) was employed to obtain the X-ray photoelectron spectra (XPS) and all data were calibrated against the C1s peak at 284.6 eV. The nitrogen sorption measurement was carried through on an ASAP 2460 (Micromeritics, USA). Field emission scanning electron microscopy (FESEM, Hitachi S-4800, Japan) was used to analyze the morphology. Atomic force microscope (AFM, Bruker Dimension Fastscan, USA) was used to obtain the thickness of TFB-TAPT nanolayer for the skin-like QSSE. Tensile and puncture strengths were obtained from Zwick Z250 tensile testing machine. Zeta potential was tested on Anton Paar surpass 3

instruments at room temperature.

1.4 Electrochemical measurements.

Zn//Zn, Zn//Cu, and Zn-I_2 batteries were assembled by CR2025 coin-type cells with 100 mL 2 M $ZnSO_4$ electrolyte (glass-fiber separator) or skin-QSSE (without separator) in the air atmosphere. Charging/discharging data of the batteries were tested with the LANDdt multi-channel battery test system at room temperature within a voltage range of 0.6 to 1.6 V. Cyclic voltammogram (CV, 0.6-1.6 V) and electrochemical impedance spectroscopy (EIS, from 100 mHz to 7 MHz) measurements were examined on electrochemical workstation (PGSTAT302N, Metrohm Autolab, China) at room temperature.

Zinc ion transference number (t_{Zn2+}) is calculated by the following formulas:

$$t_{Zn^{2+}} = \frac{(\frac{\Delta V}{I_0} - R_0)}{(\frac{\Delta V}{I_S} - R_S)}$$

where ΔV is the polarization−voltage (10 mV); I_0 is the initial current, I_S is steady-state current after polarization; R_0 and R_S are the resistances of symmetric Zn//Zn batteries before and after the polarization.

The ion conductivity of σ is calculated by the following formula:

$$\sigma = \frac{L}{RS}$$

where R is the resistance; L and S are the thickness and area skin-QSSE or separator, respectively.

The activation energy (E_a) of the Zn deposition process was calculated by monitoring the impedance (R_{ct}) of Zn//Zn symmetric batteries at different temperatures.

$$\frac{1}{R_{ct}} = \mathrm{A}\exp(-\frac{E_a}{RT})$$

where R_{ct} is the charge transfer resistance obtained from the EIS spectra, R is the gas constant and T is thermodynamic temperature.

1.5 Theoretical calculations and simulations.

Density function theory (DFT) calculations.

The calculations on electrostatic potential (ESP) and potential energy surface (PES) were conducted using the ORCA quantum chemistry program package (version 5.0.3). Density functional theory (DFT) calculation based on B3LYP functional[2] was employed in the optimization with the triple-ζ quality def2-TZVP base set[3] for all structures involved in ESP analyses. The RIJCOSX approximation[4] was employed to accelerate calculations using B3LYP functional with the def2/J auxiliary basis set.[5] For the structures used in PES calculations, optimizations were carried out using the BP functional[6] in conjunction with the def2-SVP basis set.[2] The RI approximation[7] was employed to accelerate calculations using BP functional with the set def2/J auxiliary basis. The solvation effect of water (ε = 78.355) was taken into account using the conductor-like polarizable continuum (C-PCM) model.[8] To account for dispersion effects, the Becke-Johnson damping (D3BJ) method was applied as a dispersion correction to the DFT energy.[9] For enhancing the accuracy of weak interaction energies, basis set superposition error (BSSE)[10] was taken into consideration. The ESP was evaluated using Multiwfn[11] and plotted using VMD.[12]

Molecular dynamic (MD) simulations.

To understand the ions diffusion behavior in Covalent Organic Frameworks (COFs) of skin-QSSE, molecular dynamic (MD) simulations were performed using the forcite module of Materials Studio. For the COFs, the P1 space group was employed with lattice constants: a = b = 35.1154 Å, c = 7.0136 Å, and angles α = β = 90.00°, γ = 120.00°.

First, the COFs underwent geometric optimization, forming a 2×1×1 supercell extended by 20 Å in the z-direction to accommodate the electrolyte. Next, the amorphous cell module was used to fill one side of the extended COFs with the electrolyte, which included 88 sulfate ions (SO_4^{2-}), 88 zinc ions (Zn^{2+}), 16 iodide ions (I^-), 16 triiodide ions (I_3^-), and 1800 water molecules. The filled model was then subjected to a 12 ns Microcanonical Ensemble (NVE) simulation at 298.0 K and 1 atm. The COMPASS II force field was used to compute intermolecular interactions, with charges assigned by the force field (interval=0.5 Å). Electrostatic and van der Waals

forces described by the Ewald method and a cutoff radius set to 15 Å.

The analysis of the dynamic simulation results involved calculating the radial distribution function (RDF) between different ions and cyano groups to reveal the selective permeability mechanism of the COF membrane. Additionally, the mean squared displacements (MSD) of each ion was computed to obtain the diffusion coefficients, with zinc ions in the electrolyte showing the fastest diffusion.

Finite Element Analysis.

COMSOL Multiphysics 6.2 was used to perform finite element simulations. The electrochemical potential distribution, current density distribution, and ions concentration were described in the multi-physics model of the electric field and zinc ion concentration field. Ion diffusion and migration follow Fick's first law and the Nernst-Planck equation. The skin-like QSSE electrolyte is simplified with a structure containing a gel layer and a porous channel layer. Consistent with experimental data, 2 M $ZnSO_4$ as the liquid electrolyte. The diffusion coefficient of Zn^{2+} in the electrolyte was set to 2e-9 m^2/s. The conductivities of the LE and skin-like QSSE models were set to 4.4 mS/cm and 11 mS/cm, respectively. The cathode was set at the zero potential boundary and the anode potential was set to the polarization voltage measured in the experiment with a zinc symmetric battery. At the same time, a constant current of 1 mA cm^{-2} was loaded on the upper surface of the electrolyte.

Supplementary Figures

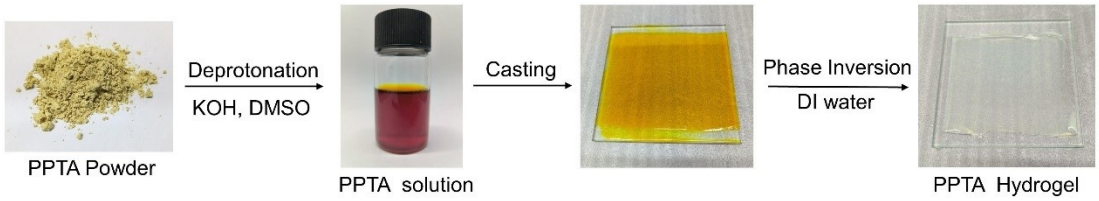

Figure S1. Fabrication of the PPTA Hydrogel by phase inversion process.

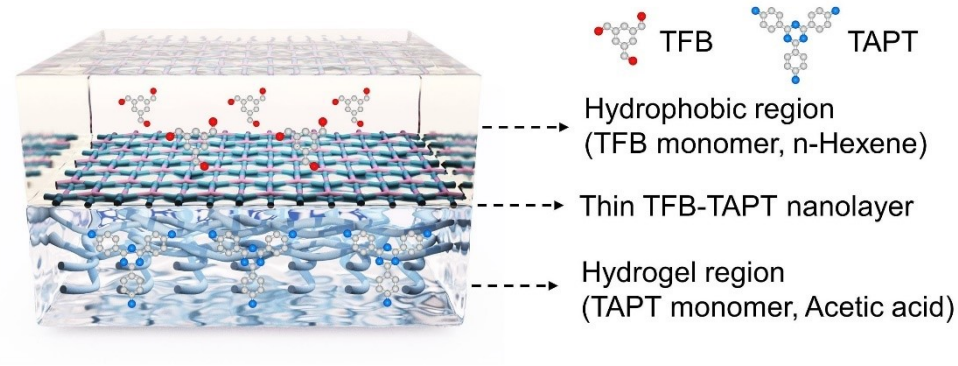

Figure S2. Schematic diagram of the COF-PPTA hydrogel at the interface between the hydrophobic region and hydrogel region.

TFB monomers and TAPT monomers were dispersed in the hydrophobic region and hydrogel region for interfacial polymerization, respectively. Acetic acid acts as a catalyst to initiate the Schiff base polycondensation reaction and promotes COF crystallization.

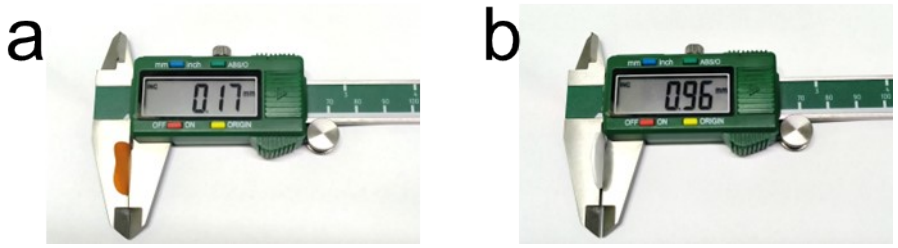

Figure S3. Thickness test for (a) the skin-QSSE and (b) glass fiber (GF).

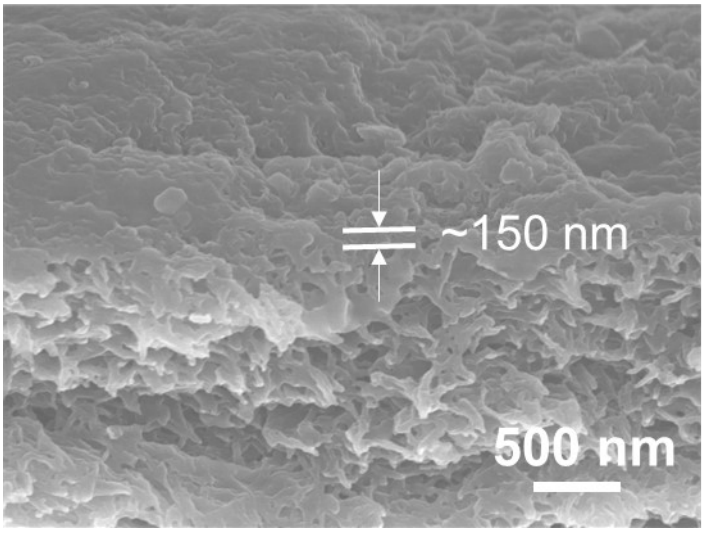

Figure S4. Cross-sectional SEM image of the skin-like QSSE.

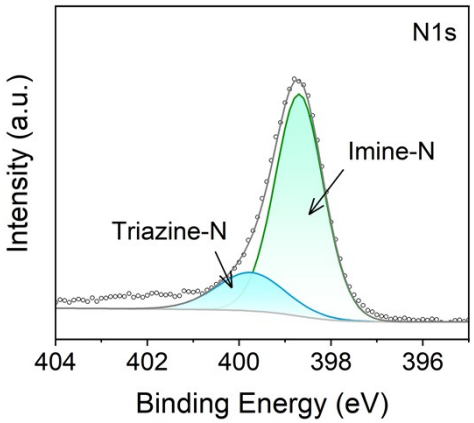

Figure S5. The high-resolution XPS spectrum of N 1s for TFB-TAPT@PPTA.

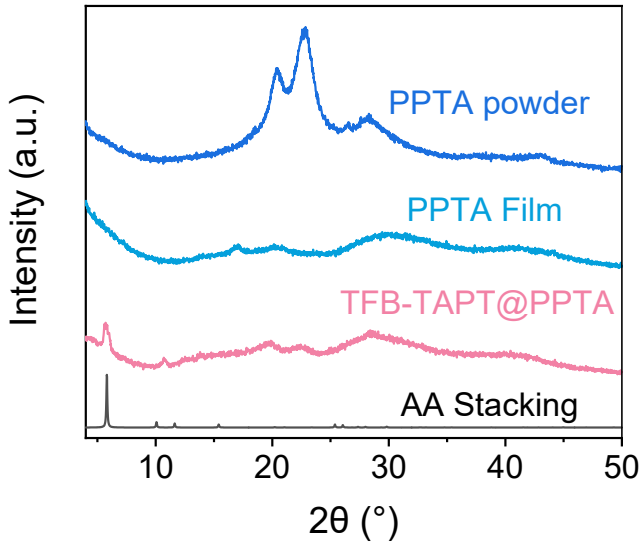

Figure S6. XRD patterns of PPTA powder, dry PPTA film, and dry TFB-TAPT@PPTA.

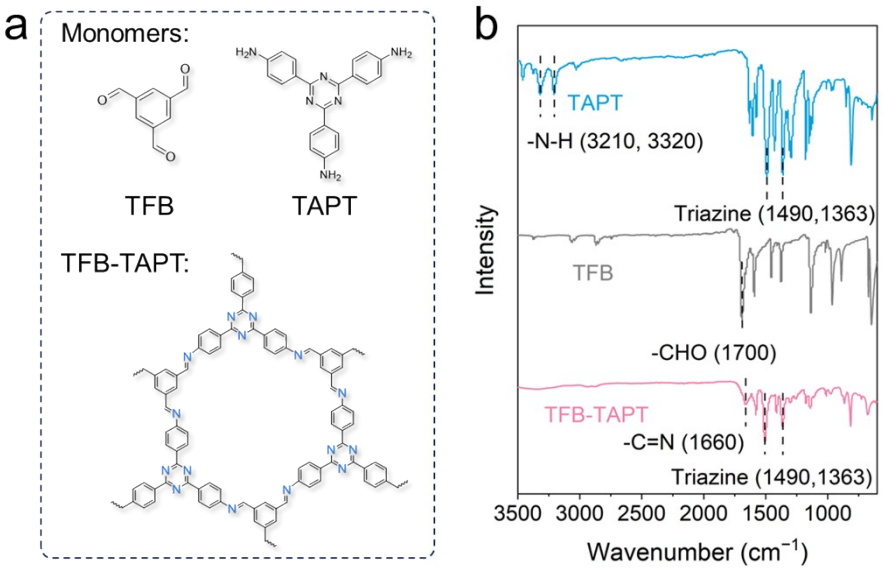

Figure S7. The (a) chemical structure and (b) FT-IR spectra of TFB-TAPT and their monomers.

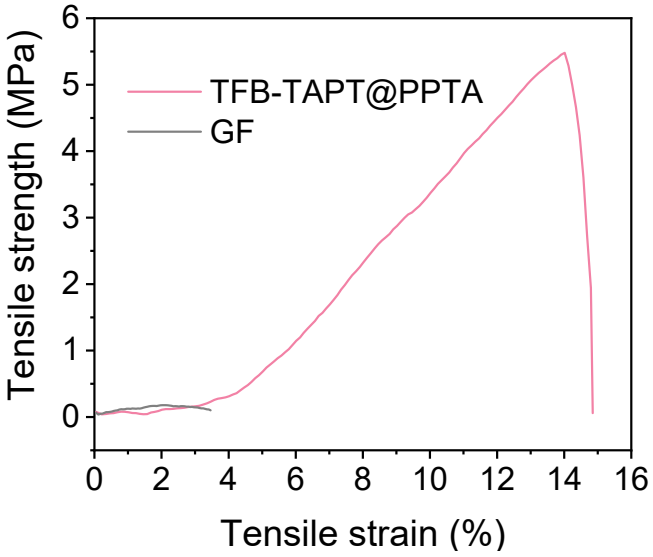

Figure S8. Tensile stress–strain curves for GF and TFB-TAPT@PPTA.

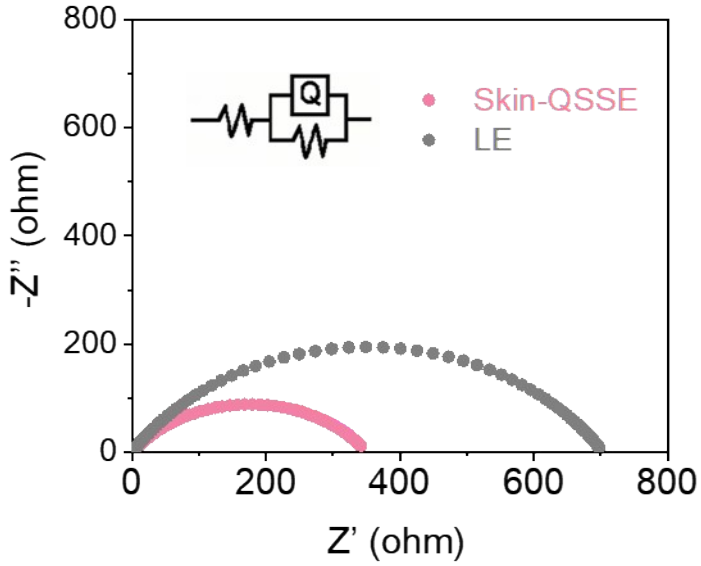

Figure S9. The electrochemical impedance spectroscopy (EIS) spectra of Zn//Zn symmetric batteries with LE and the skin-QSSE.

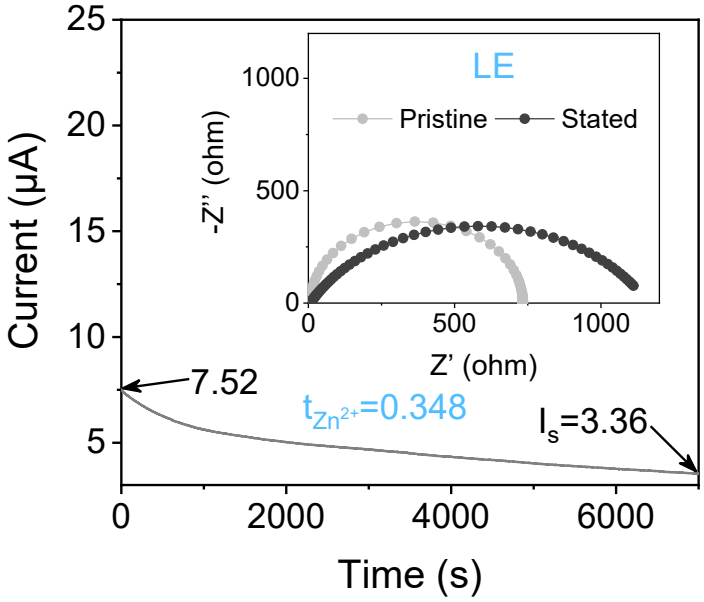

Figure S10. Nyquist plots and chronopotentiometric curve of the Zn//Zn symmetric batteries before and after polarization (ΔV=10 mV) and Zn^{2+} transference numbers in the LE.

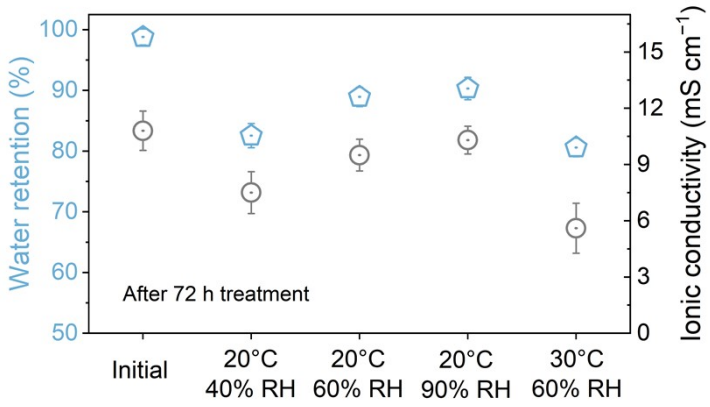

Figure S11. Water content and ionic conductivity of the skin-QSSE after 72 h treatment at different temperatures and humidity.

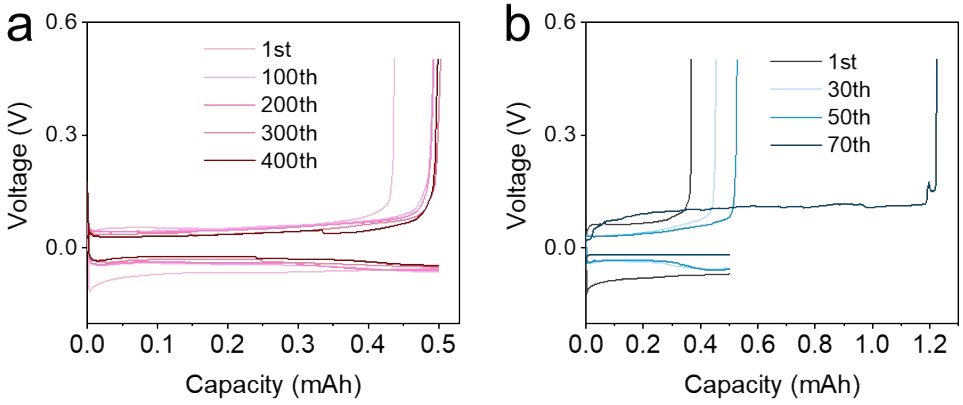

Figure S12. Capacity-voltage curves of Zn//Cu batteries using (a) the skin- QSSE and (b) LE.

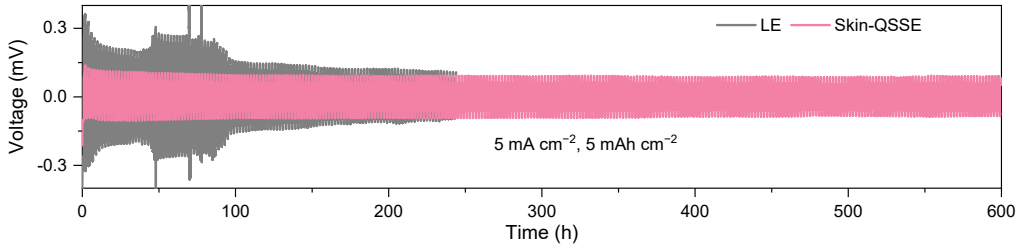

Figure S13. Cycling performance of Zn plating/stripping processes of Zn//Zn symmetric batteries with LE and skin-QSSE at 5 mA cm^{-2} (5 mAh cm^{-2}).

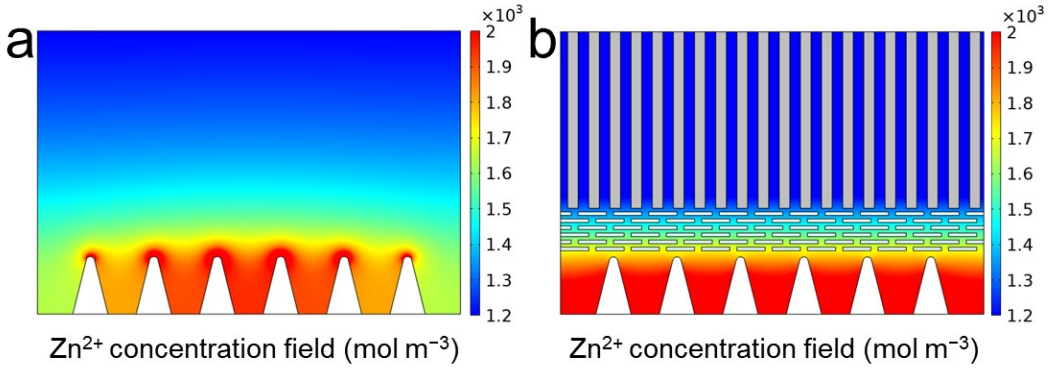

Figure S14. COMSOL simulations of Zn^{2+} concentration field with (a) LE and (b) skin-QSSE.

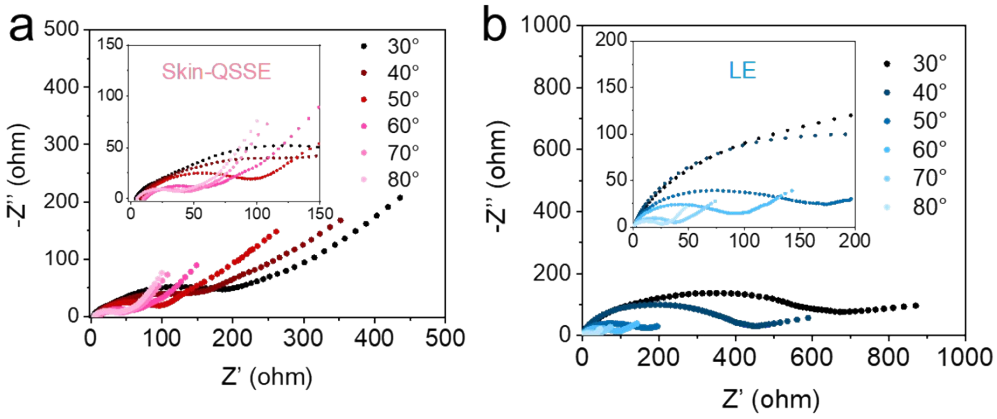

Figure S15. Nyquist plots at 30-80 °C with (a) skin-QSSE and (b) LE.

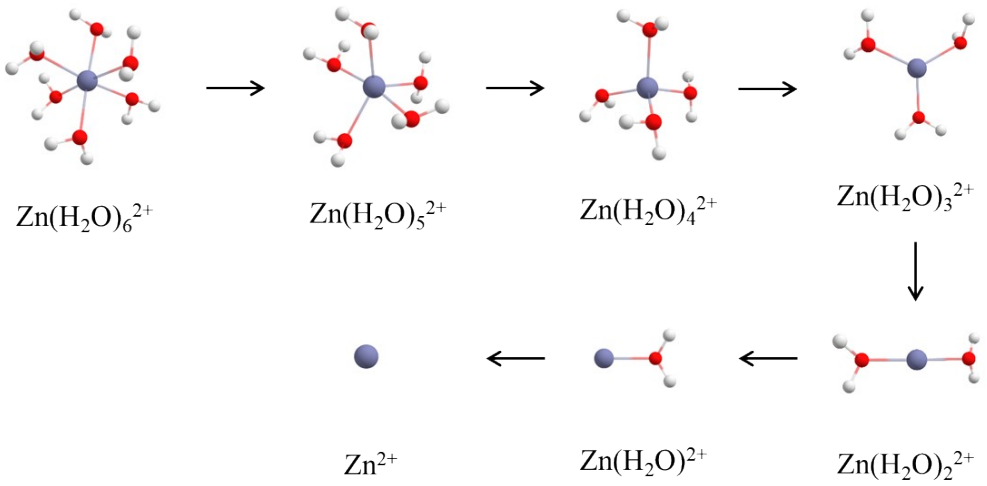

Figure S16. The configurations of hydrated zinc ion dehydration without PPTA.

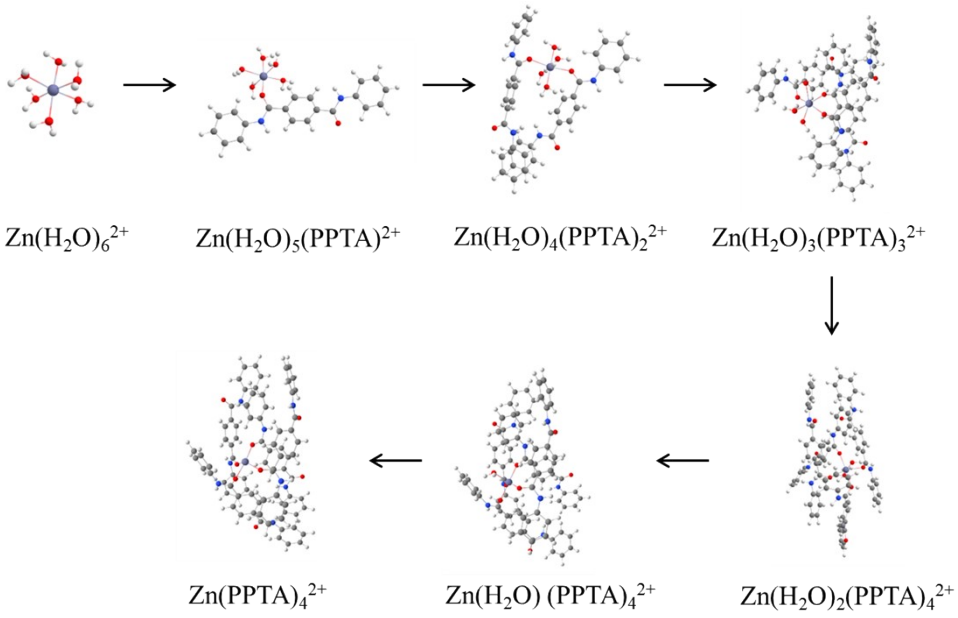

Figure S17. The configurations of hydrated zinc ion dehydration with PPTA (PPTA saturated coordination). Limited by the spatial steric hindrance of the PPTA molecular chains, up to four PPTAs are coordinated to zinc ions.

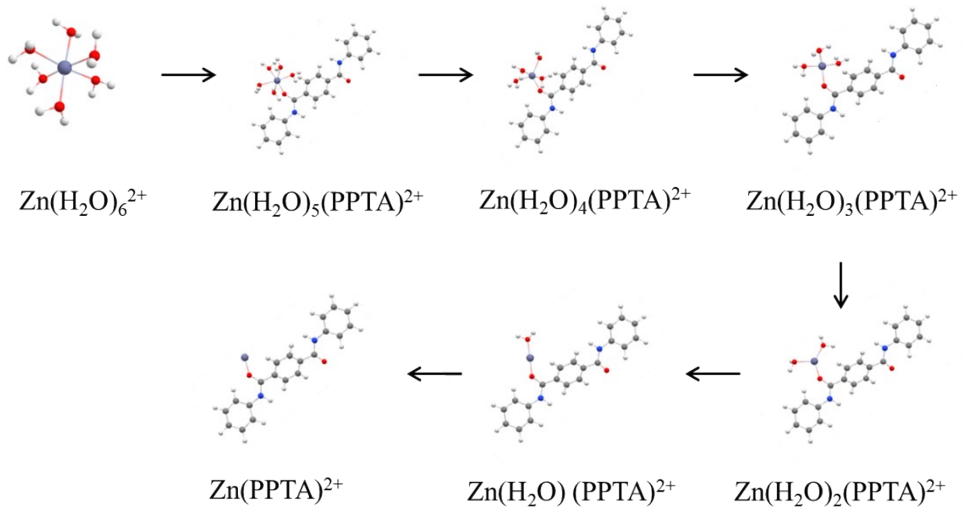

Figure S18. The configurations of hydrated zinc ion dehydration with PPTA (PPTA monocoordination). Control of one PPTA coordinated to zinc ions.

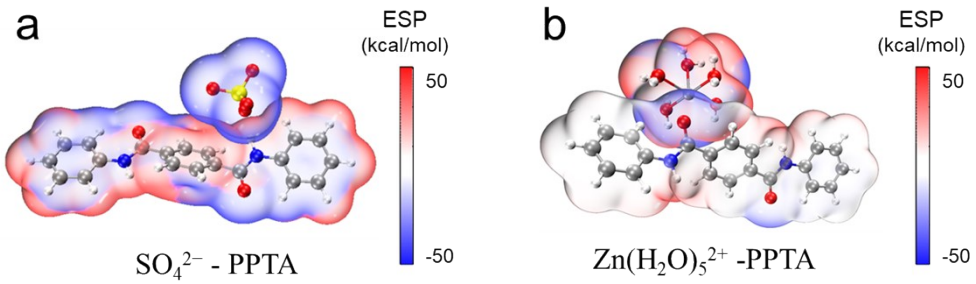

Figure S19. ESP distributions of SO_4^{2-} and $Zn(H_2O)_5^{2+}$ on PPTA.

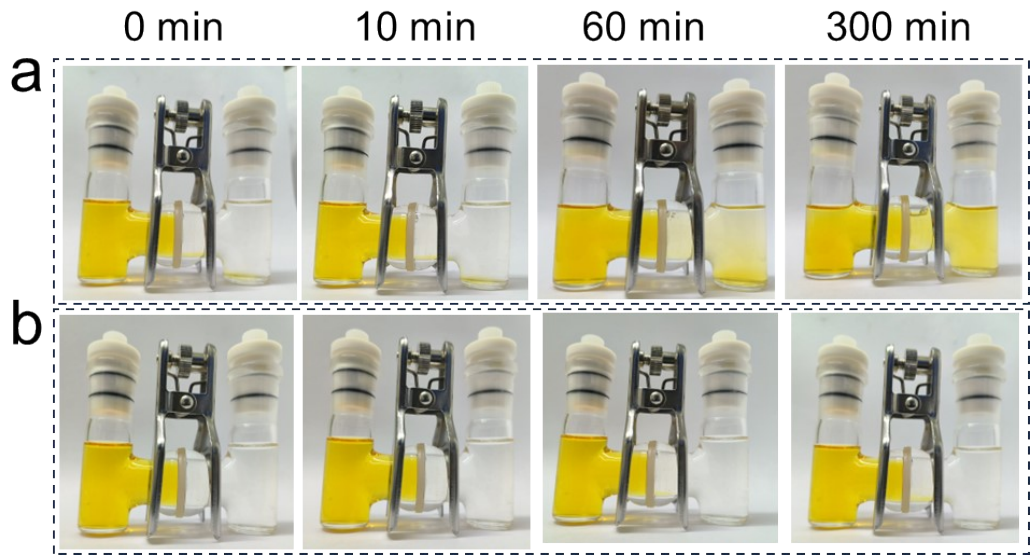

Figure S20. Visual shuttle test by H-type glass cells for (a) LE and (b) Skin-QSSE.

Visual shuttle test: H-type glass cells were employed to evaluate the barrier capabilities of Skin-QSSE toward polyiodide ions. Specifically, the left chamber of the H-cell was filled with a polyiodide solution (0.1 M ZnI_2 and 0.2 g L^{-1} I_2 solution), while the right chamber contained an equal volume of deionized water. The two chambers were separated by GF separators, QSSE and Skin-QSSE, respectively. Subsequently, the solutions in the right chamber after different times were detected by UV-visible absorption spectroscopy. The characteristic absorption peaks of I_3^- were observed at ~288 and 350 nm.

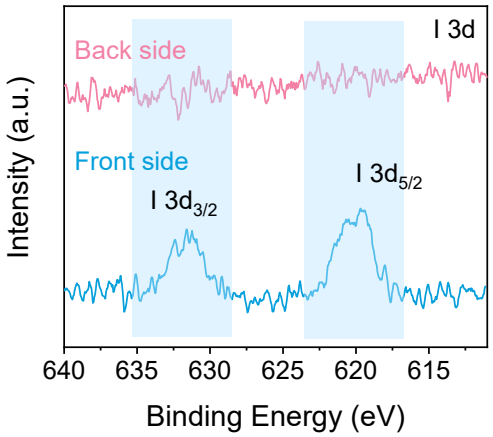

Figure S21. XPS patterns of the back side and front side for skin-like QSSE after visual shuttle test.

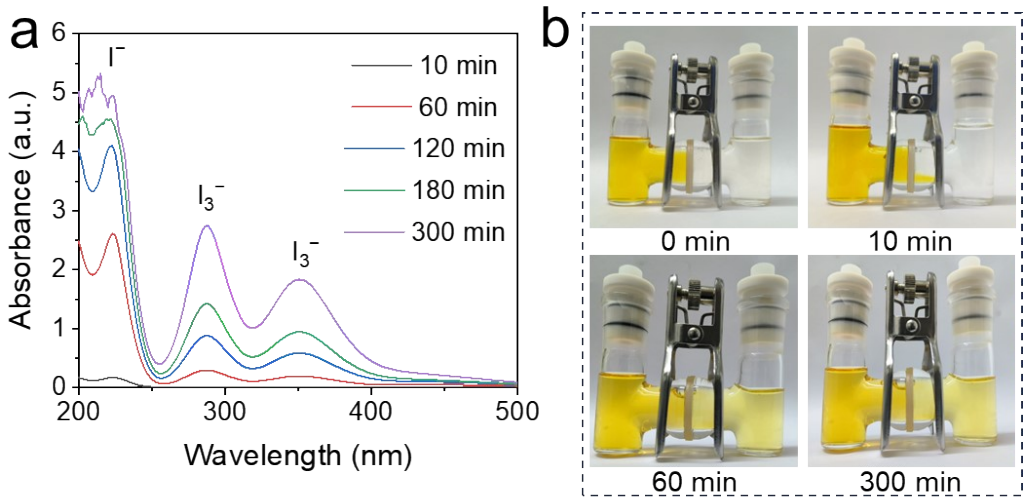

Figure S22. (a) UV-Vis absorption spectra of the right chamber and (b) visual shuttle test by H-type glass cells for QSSE without COF nanolayers.

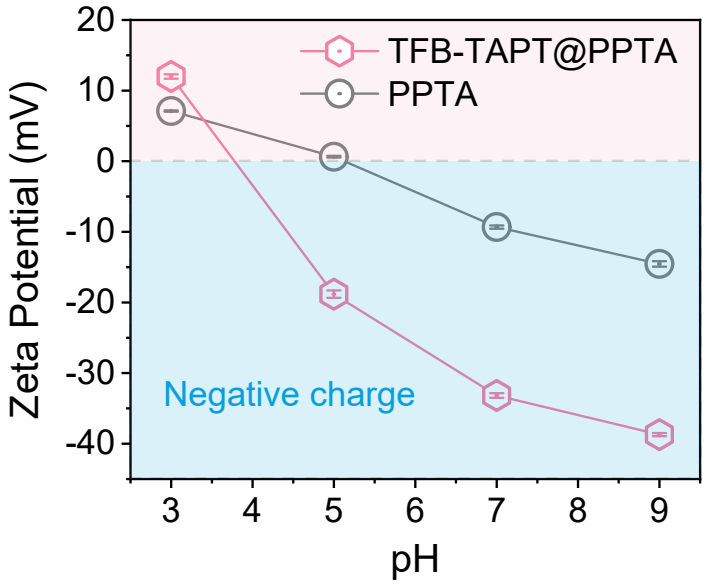

Figure S23. Zeta potentials of PPTA in the pH range of 3-9.

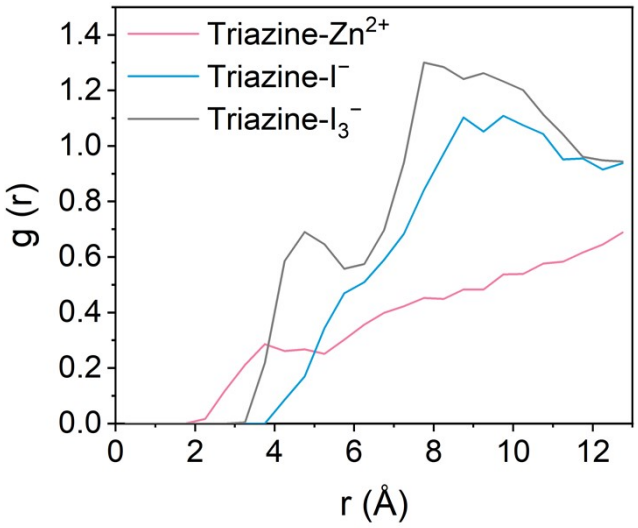

Figure S24. Radial distribution functions (RDFs) for various ions in triazine group of TFB-TAPT.

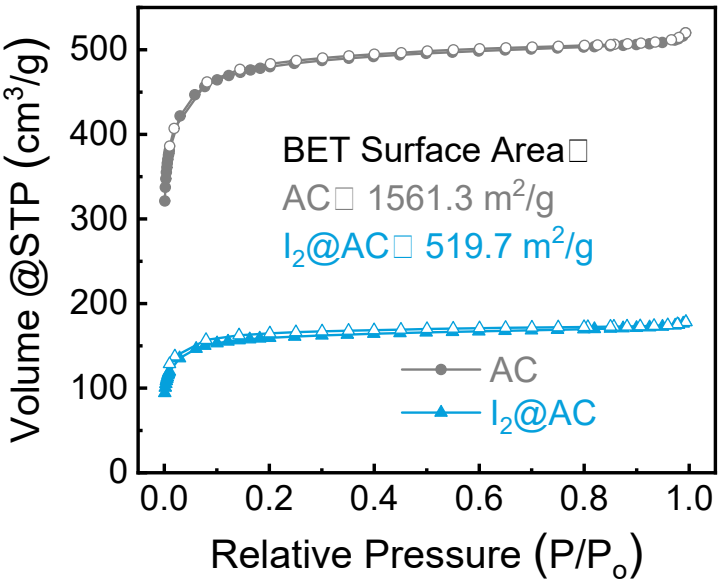

Figure S25. N_2 adsorption-desorption isotherms of AC and I_2@AC.

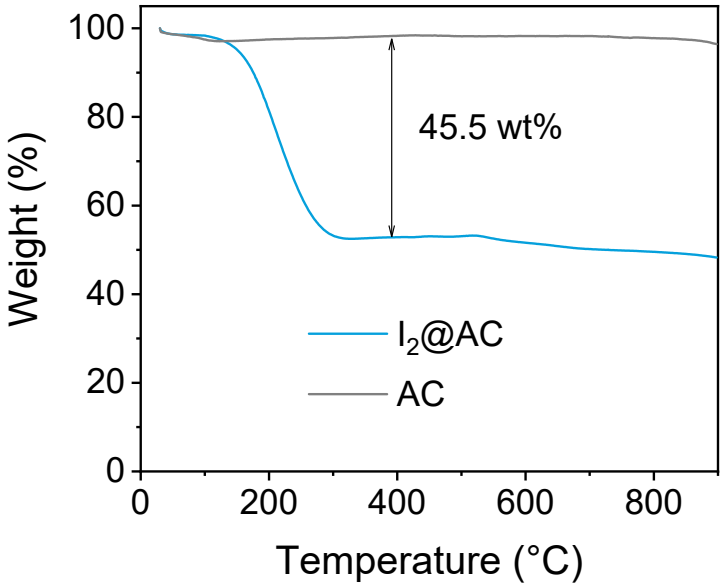

Figure S26. Thermogravimetric curves of AC and I_2@AC.

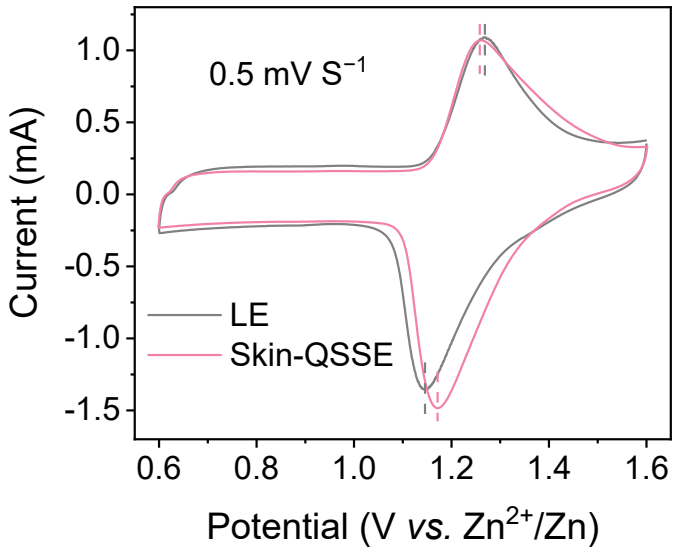

Figure S27. The cyclic voltammetry (CV) curves of Zn-I_2 batteries with LE and skin-QSSE.

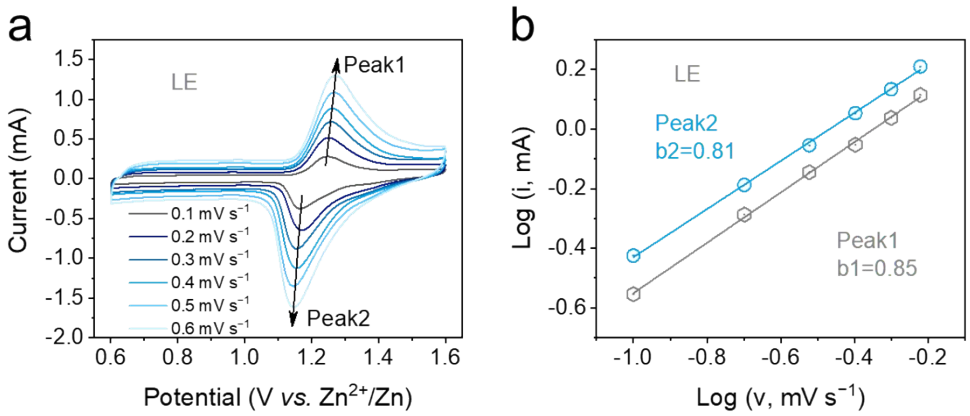

Figure S28. (a) The cyclic voltammetry (CV) curves and (b) log-linear relationship of oxidation and reduction peak currents versus scan rates of Zn-I_2 batteries with LE at different scan rates.

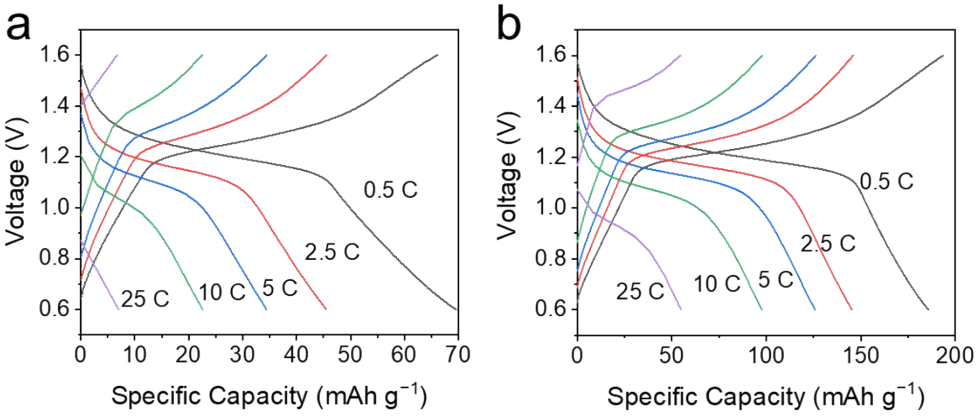

Figure S29. The galvanostatic charge–discharge (GCD) curves of the Zn-I_2 batteries assembled by (a) LE and (b) skin-QSSE at differences C-rates.

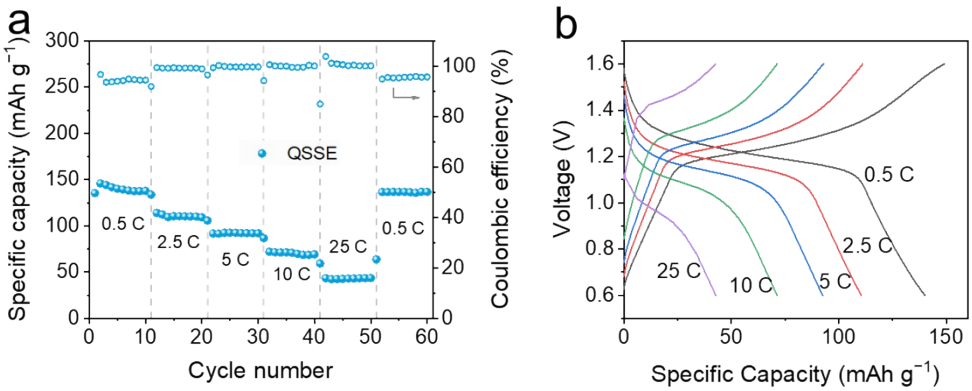

Figure S30. (a) Rate performance of the Zn-I_2 batteries assembled by QSSE without TFB-TAPT nanolayer and (b) the GCD curves at differences C-rates.

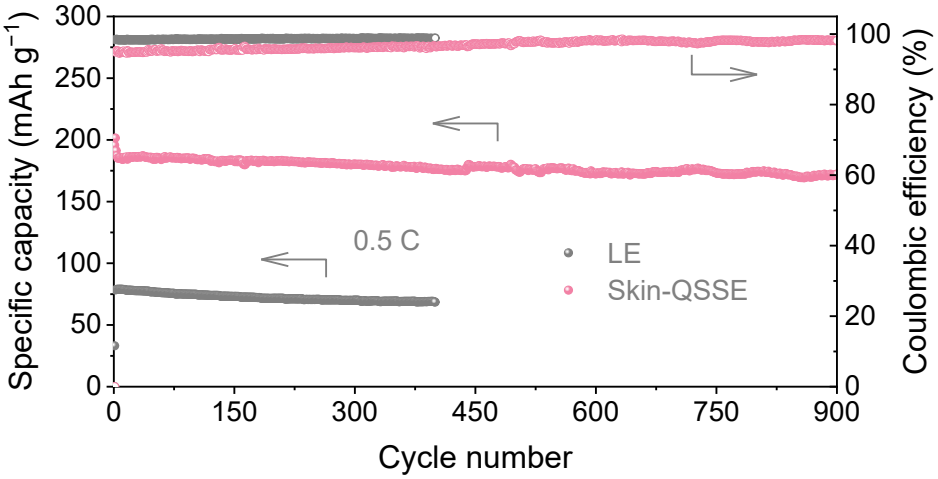

Figure S31. Long-term cycling performance for Zn-I_2 batteries with LE and skin-QSSE at 0.5 C.

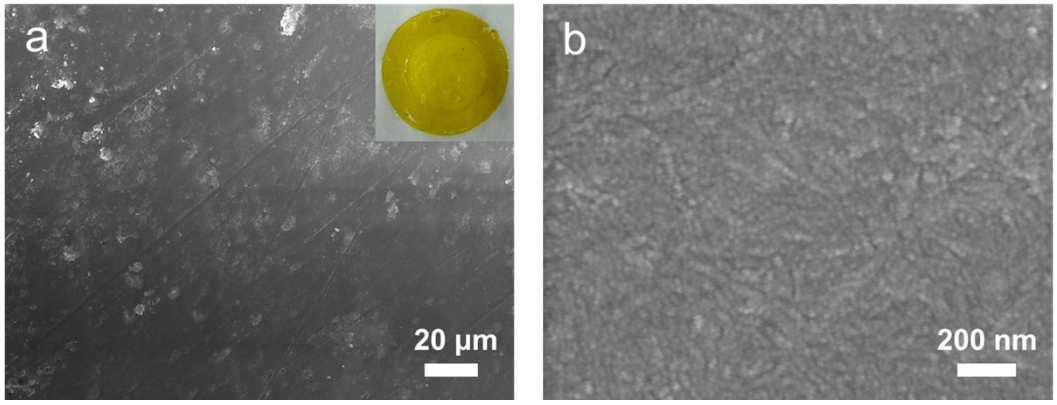

Figure S32. SEM images of different magnifications for the skin-QSSE after cycling in the Zn-I_2 battery (inset: optical photograph for the skin-QSSE).

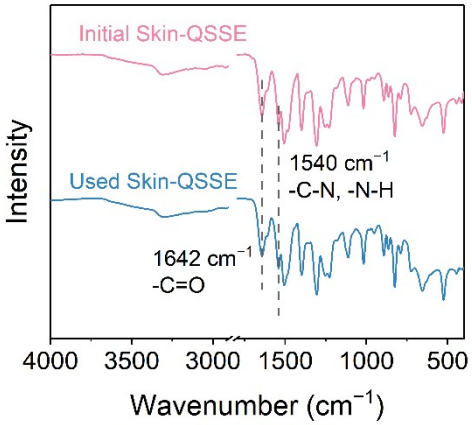

Figure S33. FT-IR spectra of initial skin-QSSE and used skin-QSSE after 100 h cycling.

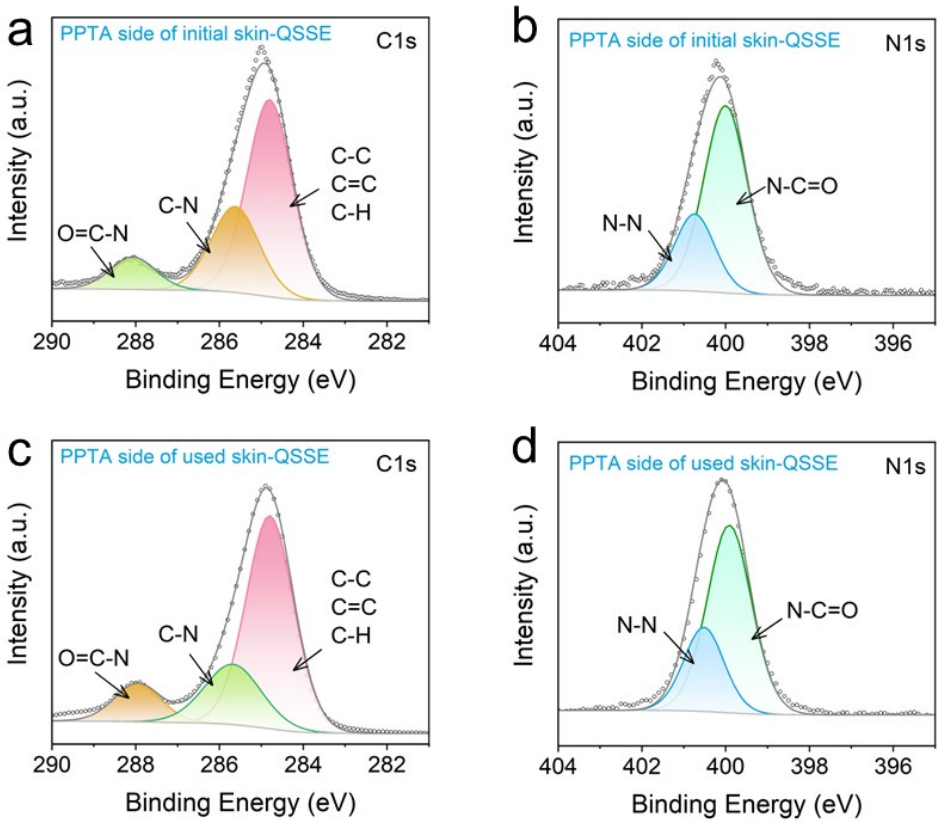

Figure S34. High-resolution spectra of PPTA side of initial skin-QSSE (a, b) and used skin-QSSE (c, d) after cycling.

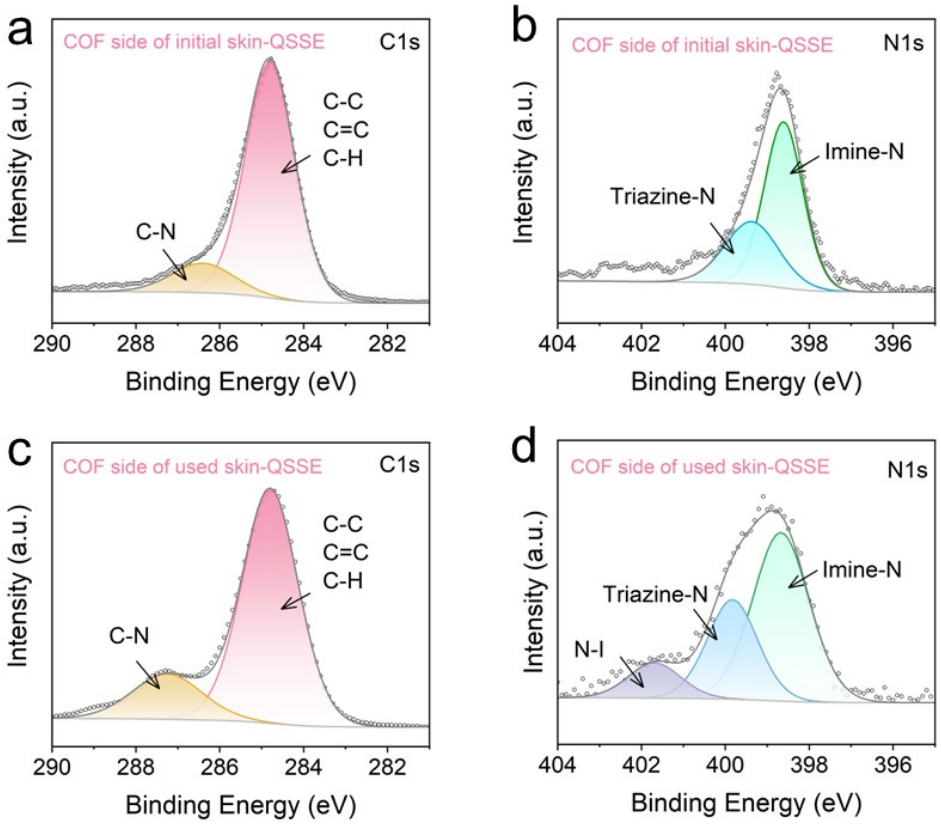

Figure S35. High-resolution spectra of COF side of initial skin-QSSE (a, b) and used skin-QSSE (c, d) after cycling.

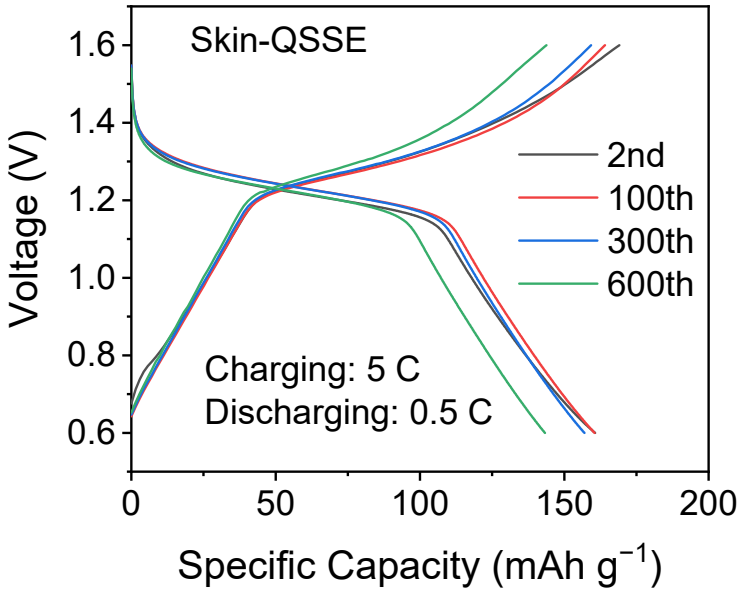

Figure S36. The GCD curves of the Zn-I_2 batteries assembled by skin-QSSE of fast-charging and slow-discharging process.

Figure S37. Digital photos of a Zn-I_2 pouch battery with skin-QSSE.

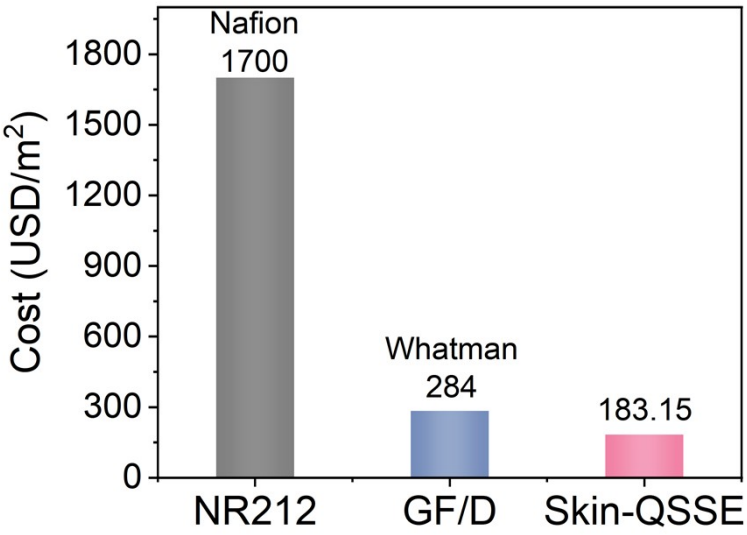

Figure S38. A comparison of the material costs for producing skin-QSSE and commercial separators.

Supplementary Tables

Table S1. Comparison of this work with reported performance of Zn/I_2 batteries based on electrolyte or separator design.

Electrolyte	Specific capacity (mA h g^{-1})	Current density	Cycling number	Capacity retention (%)	Capacity decay rate (‰)	Ref.
$ZnBF_4$-SN eutectic electrolytes	180	2 A g^{-1} 10 A g^{-1}	1000 10000	82 75	0.18 0.025	[13]
Alginate hydrogel	214.7 120.8	0.2 A g^{-1} 2 A g^{-1}	150 2000	98.3 66.8	0.1133 0.166	[14]
$ZnSO_4$-PG eutectic electrolytes	210	1 C 5 C	150 2000	97.9	0.0105	[15]
i-HNTs@PAM gel electrolytes	215.8 180	1 C 8 C	400 8000	97.1 88.2	0.0725 0.0148	[16]
PAH/PCH Hetero-Polyionic Hydrogels	175 128	2 C 8 C	2500 18000	93.7 85.6	0.0252 0.008	[17]
$Zn(ClO_4)_2$-ACN electrolyte	169	10 C	5000	93	0.014	[18]
Zn-PCA	211	1 A g^{-1} 10 A g^{-1}	100 30000	99 87	0.1 0.0043	[19]
EI-ZrP	140	20 C	10000	80	0.02	[20]
$ZnSO_4$ with VS	253.5	5 C	13000	91	0.0069	[21]
ZPS electrolyte	154.2	0.1 A g^{-1}	400	68.7	0.7825	[22]
ZIB/CCH electrolyte	205 74	2 C 10 C	2000 22000	82.9 83.28	0.0855 0.0076	[23]
pyridine-$ZnSO_4$	138.8	2 A g^{-1}	10000	92	0.008	[24]
IC–Zn gel electrolyte	~175	5 C	5000	91.88	0.0162	[25]
DCZ-gels electrolyte	108	2 A g^{-1}	2000	85	0.075	[26]
ACE-10 Separator	/	1 C 2 C 5 C	1400 2500 10000	88.5 86.0 84.8	0.0821 0.056 0.0152	[27]
Zn-BTC membrane	201.1 85.1	0.16 A g^{-1} 1.92 A g^{-1}	100 6000	99 84.6	0.1 0.0257	[28]
Dowex+Fe-SCNT/GF	/	5 A g^{-1}	30000	76	0.008	[29]

separator						
Skin-like QSSE	201.5 133.8 126.2	0.5 C 5 C 10 C	900 15000 45000	85.5% 89.2% 92.0%	0.16 0.0072 0.0018	This work

1 C = 0.211 A g^{-1}

Table S2. Estimated primary material costs assessment for production of the skin-QSSE.

Materials	PPTA fiber	DMSO	TFB monomer	TAPT monomer	Others	Total
Costs (USD/m^2)	1.90	19.00	99.09	61.16	~2	183.15

Others: Including KOH, acetic acid, and DI water.

References

1. Q. Zhao, Y. Lu, Z. Zhu, Z. Tao and J. Chen, *Nano Lett*, 2015, **15**, 5982-5987.
2. A. D. J. T. J. o. c. p. Becke, *J. Chem. Phys*, 1992, **96**, 2155-2160.
3. F. Weigend and R. Ahlrichs, *Phys. Chem. Chem. Phys*, 2005, **7**, 3297-3305.
4. F. Neese, F. Wennmohs, A. Hansen and U. J. C. P. Becker, *J. Chem. Phys*, 2009, **356**, 98-109.
5. K. Eichkorn, O. Treutler, H. Öhm, M. Häser and R. J. C. p. l. Ahlrichs, *Chem. Phys. Lett*, 1995, **240**, 283-290.
6. A. D. J. P. r. A. Becke, *Phys Rev A*, 1988, **38**, 3098.
7. K. Eichkorn, F. Weigend, O. Treutler and R. J. T. C. A. Ahlrichs, *Theor. Chem. Acc.*, 1997, **97**, 119-124.
8. V. Barone and M. J. T. J. o. P. C. A. Cossi, *J. Phys. Chem*, 1998, **102**, 1995-2001.
9. A. D. Becke and E. R. J. T. J. o. c. p. Johnson, *J. Chem. Phys*, 2005, **123**.
10. S. F. Boys and F. J. M. p. Bernardi, *Mol. Phys.*, 1970, **19**, 553-566.
11. T. Lu and F. Chen, *J. Comput. Chem.*, 2012, **33**, 580-592.
12. W. Humphrey, A. Dalke and K. J. J. o. m. g. Schulten, *J. Mol. Graph*, 1996, **14**, 33-38.
13. H. Xu, R. Zhang, D. Luo, J. Wang, K. Huang, J. Chi, H. Dou, X. Zhang and G. Sun, *Energy Stor. Mater.*, 2023, **63**.
14. W. Shang, J. Zhu, Y. Liu, L. Kang, S. Liu, B. Huang, J. Song, X. Li, F. Jiang, W. Du, Y. Gao and H. Luo, *ACS Appl. Mater. Interfaces*, 2021, **13**, 24756-24764.
15. J. Hao, L. Yuan, C. Ye, D. Chao, K. Davey, Z. Guo and S.-Z. Qiao, 2021, **60**, 7366-7375.
16. C.-C. Kao, J. Liu, C. Ye, S.-J. Zhang, J. Hao and S.-Z. Qiao, *J. Mater. Chem. A*, 2023, **11**, 23881-23887.
17. J. L. Yang, Z. Yu, J. Wu, J. Li, L. Chen, T. Xiao, T. Xiao, D. Q. Cai, K. Liu, P. Yang and H. J. Fan, *Adv. Mater.*, 2023, **35**, e2306531.
18. C. Song, Z. Gong, C. Bai, F. Cai, Z. Yuan and X. J. N. R. Liu, *Nano Research*, 2022, 1-8.
19. F. Wang, W. Liang, X. Liu, T. Yin, Z. Chen, Z. Yan, F. Li, W. Liu, J. Lu, C. Yang and Q. H. Yang, *Adv. Energy Mater.*, 2024, DOI: 10.1002/aenm.202400110.
20. J. Wu, J. L. Yang, B. Zhang and H. J. Fan, *Adv. Energy Mater.*, 2023, **14**.
21. G. Chen, Y. Kang, H. Yang, M. Zhang, J. Yang, Z. Lv, Q. Wu, P. Lin, Y. Yang and J. Zhao, *Adv. Funct. Mater.*, 2023, **33**.
22. Z. Lv, Y. Kang, G. Chen, J. Yang, M. Chen, P. Lin, Q. Wu, M. Zhang, J. Zhao and Y. Yang, *Adv. Funct. Mater.*, 2023, **34**.
23. J. L. Yang, T. Xiao, T. Xiao, J. Li, Z. Yu, K. Liu, P. Yang and H. J. Fan, *Adv. Mater.*, 2024, DOI: 10.1002/adma.202313610, e2313610.
24. Y. Lyu, J. A. Yuwono, P. Wang, Y. Wang, F. Yang, S. Liu, S. Zhang, B. Wang, K. Davey, J. Mao and Z. Guo, *Angew. Chem. Int. Ed.*, 2023, **62**, e202303011.
25. Y. Tian, S. Chen, S. Ding, Q. Chen and J. Zhang, *Chem Sci*, 2023, **14**, 331-337.
26. H. Zhang, X. Gan, Y. Yan and J. Zhou, *Nanomicro Lett*, 2024, **16**, 106.
27. P. Lin, G. Chen, Y. Kang, M. Zhang, J. Yang, Z. Lv, Y. Yang and J. Zhao, *ACS Nano*, 2023, **17**, 15492-15503.
28. H. Yang, Y. Qiao, Z. Chang, H. Deng, P. He and H. Zhou, *Adv. Mater.*, 2020, **32**, e2004240.
29. Y. Kang, G. Chen, H. Hua, M. Zhang, J. Yang, P. Lin, H. Yang, Z. Lv, Q. Wu, J. Zhao and Y. Yang, *Angew. Chem. Int. Ed.*, 2023, **62**, e202300418.